Eur. Phys. J. C (2022) 82:1112
https://doi.org/10.1140/epjc/s10052-022-11069-3

THE EUROPEAN PHYSICAL JOURNAL C

Regular Article - Experimental Physics

Calibration strategy of the JUNO-TAO experiment

Hangkun Xu[1,2], Angel Abusleme[3,4], Nikolay V. Anfimov[13], Stéphane Callier[8], Agustin Campeny[3], Guofu Cao[1,2], Jun Cao[1,2], Cedric Cerna[7], Yu Chen[5], Alexander Chepurnov[15], Yayun Ding[1,2], Frederic Druillole[7], Andrea Fabbri[12], Zhengyong Fei[1,2], Maxim Gromov[14,15], Miao He[1,2], Wei He[1,2], Yuanqiang He[5], Joseph Y. K. Hor[5], Shaojing Hou[2], Jianrun Hu[1,2], Jun Hu[2], Cédric Huss[7], Xiaolu Ji[1,2], Tao Jiang[5], Xiaoshan Jiang[1,2], Cécile Jolliet[7], Daozheng Li[2], Min Li[1,2], Ruhui Li[1,2], Yichen Li[1,2], Caimei Liu[2], Mengchao Liu[2], Yunzhe Liu[1,2], Claudio Lombardo[11], Selma Conforti Di Lorenzo[8], Peizhi Lu[5], Guang Luo[5], Stefano M. Mari[12], Xiaoyan Ma[1,2], Paolo Montini[12], Juan Pedro Ochoa-Ricoux[3], Yatian Pei[1,2], Frédéric Perrot[7], Fabrizio Petrucci[12], Xiaohui Qian[1,2], Abdel Rebii[7], Bedřich Roskovec[6], Arsenij Rybnikov[13], Hans Steiger[9,10], Xilei Sun[1,2], Pablo Walker[3], Derun Wang[1,2], Meifen Wang[2], Wei Wang[5], Wei Wang[2], Zhimin Wang[1,2], Diru Wu[1,2], Xiang Xiao[5], Yuguang Xie[1,2], Zhangquan Xie[1,2], Wenqi Yan[1,2], Huan Yang[2], Haifeng Yao[1,2], Mei Ye[1,2], Chengzhuo Yuan[1,2], Kirill Zamogilnyi[16], Liang Zhan[1,2,a], Jie Zhang[1,2], Shuihan Zhang[2], Rong Zhao[5]

[1] University of Chinese Academy of Sciences, Beijing, China
[2] Institute of High Energy Physics, Beijing, China
[3] Pontificia Universidad Católica de Chile, Santiago, Chile
[4] Millennium Institute for Subatomic Physics at High-Energy Frontier-SAPHIR, Santiago, Chile
[5] Sun Yat-sen University, Guangzhou, China
[6] Faculty of Mathematics and Physics, Charles University, Prague, Czech Republic
[7] Centre d'Etudes Nucléaires de Bordeaux-Gradignan, Gradignan, France
[8] Organisation de MicroÉlectronique Générale Avancée, Palaiseau, France
[9] Physik-Department, Technische Universitä München, James-Franck-Str. 1, Garching, Germany
[10] Cluster of Excellence PRISMA+ and Institute of Physics, Detector Laboratory, Staudingerweg 9, Mainz, Germany
[11] INFN Catania and Dipartimento di Fisica e Astronomia dell'Universitá di Catania, Catania, Italy
[12] Istituto Nazionale di Fisica Nucleare Sezione di Roma Tre, Rome, Italy
[13] Joint Institute for Nuclear Research, Dubna, Russia
[14] Moscow State University, Moscow, Russia
[15] Skobeltsyn Institute of Nuclear Physics, Lomonosov Moscow State University, Moscow, Russia
[16] Faculty of Physics, Lomonosov Moscow State University, Moscow, Russia

Received: 31 May 2022 / Accepted: 23 November 2022 / Published online: 9 December 2022

Abstract The Taishan Antineutrino Observatory (TAO or JUNO-TAO) is a satellite experiment of the Jiangmen Underground Neutrino Observatory (JUNO). Located near a reactor of the Taishan Nuclear Power Plant, TAO will measure the reactor antineutrino energy spectrum with an unprecedented energy resolution of $< 2\%$ at 1 MeV. Energy calibration is critical to achieve such a high energy resolution. Using the Automated Calibration Unit (ACU) and the Cable Loop System (CLS), multiple radioactive sources are deployed to various positions in the TAO detector for energy calibration. The residual non-uniformity can be controlled within 0.2%. The energy resolution degradation and energy bias caused by the residual non-uniformity can be controlled within 0.05% and 0.3%, respectively. The uncertainty of the non-linear energy response can be controlled within 0.6% with the radioactive sources of various energies, and could be further improved with cosmogenic ^{12}B which is produced by the interaction of cosmic muon in the liquid scintillator. The stability of other detector parameters, e.g., the gain of each Silicon Photomultiplier, will be monitored with an ultraviolet LED calibration system.

1 Introduction

Detection of reactor antineutrinos with Liquid Scintillator (LS) detectors has played an important role in the development of neutrino physics [1–6]. It is also the approach used in Jiangmen Underground Neutrino Observatory (JUNO) [7] as a next-generation neutrino experiment. Reactor antineu-

[a] e-mail: zhanl@ihep.ac.cn (corresponding author)

trinos are usually detected via the Inverse Beta Decay (IBD) reaction, $\bar{\nu}_e + p \rightarrow e^+ + n$. The positron deposits its kinetic energy in the LS, then annihilates immediately with an electron and emits mostly two back-to-back 0.511 MeV gammas. The neutron scatters in the detector until it is thermalized and captured on a nucleus. Subsequently, the nucleus de-excites with the emission of gamma or alpha particles. Since the neutron capture happens about 30 μs after the positron annihilation, an IBD reaction produces a prompt and a delayed signal in the detector. This time correlation of the prompt and delayed signals is powerful to distinguish the signal from the backgrounds. The kinetic energy of the neutron is negligible. The initial $\bar{\nu}_e$ energy can be approximately calculated as $E_{\bar{\nu}_e} \approx E_{\text{prompt}} + 0.784\text{MeV}$ [8], where E_{prompt} is the sum of the positron kinetic energy and the annihilation energy.

In a liquid scintillator detector, charged particles interact with the liquid scintillator and release photons. The number of detected photons depends on the position of the charged particle. This is caused by the attenuation of the photons in the liquid scintillator, the total acceptance angle of the photon detectors, the reflection from the material surface, and so on [9]. The position dependence of the number of detected photons is called detector non-uniformity and is generally independent of the particle energy. In addition, the number of emitted photons is not proportional to the kinetic energy of the charged particle. This effect is referred to as the "physics non-linearity" and is mainly caused by the ionization quenching and Cherenkov radiation [8]. Non-uniformity and non-linearity could compromise the measurement of the antineutrino energy spectrum. Therefore, both effects need to be corrected by calibration.

The Taishan Antineutrino Observatory (JUNO-TAO, or TAO) is a satellite experiment of JUNO. It is located at 30 m from a reactor core of the Taishan Nuclear Power Plant and detects reactor antineutrinos with 2.8 tons Gadolinium-doped Liquid Scintillator (GdLS). The primary physics goal of JUNO is to determine the neutrino mass ordering by measuring the reactor antineutrino spectrum with an energy resolution of better than $3\%/\sqrt{\text{E(MeV)}}$ [7]. TAO will measure the reactor antineutrino spectrum with an energy resolution of better than 2% at 1 MeV to provide a model-independent reference spectrum for JUNO and a benchmark measurement to test nuclear databases. Achieving these goals requires less than 1% uncertainty in the physics non-linearity and less than 0.5% residual non-uniformity after correction [10]. In this paper, we present a calibration strategy that meets these requirements.

The organization of this paper is as follows. In Sect. 2, we introduce the TAO experiment and present the conceptual design of the calibration system. In Sect. 3, we discuss the details of calibration sources. In Sect. 4, we develop a method to correct the non-uniformity in the TAO detector and verify its effectiveness through simulations. In Sect. 5, we discuss the approach to calibrate the physics non-linearity and verify it through simulations. Finally, we give a conclusion in Sect. 6.

2 The calibration system of the TAO experiment

2.1 The TAO experiment

As shown in Fig. 1, TAO consists of the Central Detector (CD), the calibration system, the outer shielding and the veto system. In the CD, there is a spherical acrylic vessel with an inner diameter of 1.8 m, which contains approximately 2.8 tons of GdLS. The acrylic vessel is viewed by about 10 m^2 Silicon Photo-multipliers (SiPMs) with a photon detection efficiency of $\sim$ 50%. To reduce the dark noise of the SiPMs, the detector will operate at $-$ 50 °C. To fully contain the energy deposition of gammas from IBD positron annihilation, events within 25 cm to the edge of the acrylic vessel are excluded in the IBD selection, resulting in a fiducial volume (FV) with a diameter of 1.3 m. Full detector simulation shows about 4500 photoelectrons (PE) per MeV can be detected by SiPMs, leading to an energy resolution of about 2% at 1 MeV. TAO is able to achieve a vertex resolution of better than 5 cm using the recorded charge and timing information by the SiPMs and the electronics system [10].

2.2 Calibration system

The calibration system contains the Automated Calibration Unit (ACU), which is reused and modified from the Daya Bay experiment [11], and a Cable Loop System (CLS), as shown in Fig. 1. A segment of the CLS cable is located in the GdLS with the start point marked as P_0. A coordinate system is defined with the origin at the center of the central detector and the Z-axis pointing upwards. The ACU and CLS calibrate the energy response on and off the central axis (Z-axis), respectively.

As shown in Fig. 2a, the ACU consists of a turntable and three mechanically independent motor/pulley/wheel assemblies. The turntable comprises two plates (named as top and middle plates) and three assemblies mounted on the top plate. Each assembly is capable of deploying a source into the detector along the central Z-axis once the turntable rotates to a specific angle, similar to the applications in Daya Bay and JUNO [11,12]. An ultraviolet (UV) light source, a ^{68}Ge source, and a combined source that contains multiple gamma sources and one ^{241}Am-^{13}C neutron source will be installed on three assemblies, one source for each assembly.

The ^{68}Ge source and the combined source consist of radioactive materials and a stainless steel enclosure with Teflon coating, as shown in Fig. 2b. The Teflon coating reduces the absorption of light by the source with high reflec-

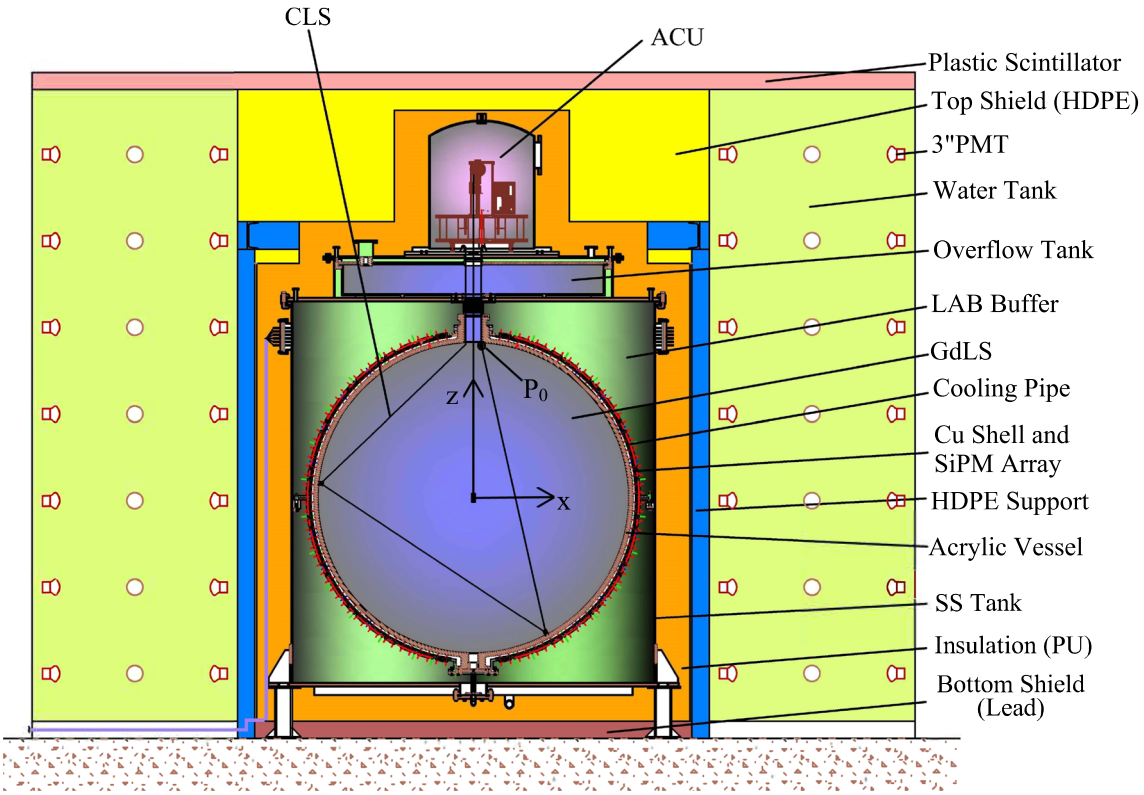

Fig. 1 Schematic of the TAO detector, which consists of the central detector, the calibration system, the outer shielding, and the veto system. The Calibration system consists of an Automated Calibration Unit (ACU) and a Cable Loop System (CLS). A segment of the CLS cable is located in the GdLS with the start point marked as P_0. A coordinate system is defined with the origin at the center of the central detector and the Z-axis pointing upwards

tivity of 95% [13]. In addition, Teflon is compatible with GdLS while stainless steel is not. Each source has two counterweights with a mass of about 40 g, which allows the wire to maintain tension when the source is deployed into the liquid scintillator. When ^{68}Ge and the combined source are parked in the ACU, they are placed within a stainless steel shield and a Borated Polyethylene (BPE) shield respectively as shown in Fig. 2a. These two shields are cylinders with a wall thickness of 2.25 inch and a height of 5 inch. Below the BPE shield, there is another BPE disk with a diameter of 3.25 inch and a height of 6.4 inch. These shields decrease the probability of the radiation of the sources going into the GdLS to a negligible level compared to other backgrounds in the TAO detector.

The UV light source is equipped with a high-OH silica optical fiber with a core diameter of 400 μm and a diffuser made of ultrapure quartz that improves the isotropy of the source's radiation. The wavelength of the UV light source is 265 nm by default. It can be changed to 420 nm or any other values by the envisaged simplified replacement of one or two LEDs in the optoelectronic unit, which is located outside the detector shielding. The UV light source is used to monitor the stability of the parameters of the TAO detector. This task includes monitoring the state of each SiPM channel and calibrating its timing, gain, and quantum efficiency. The UV light source can also be used to test the data acquisition and offline analysis pipeline and to study the event pileup in the CD.

The CLS allows us to calibrate the detector response in the off-central axis region. It adopts experience from the JUNO CLS [9,14]. The CLS includes two stepper motors, two anchors, a stainless steel cable, load cells, and limit switches. All components can work at low temperatures down to $-60\,^{\circ}$C. The radioactive source (^{137}Cs) is plated on a small area of the stainless steel cable, and the cable is covered with a 0.1 to 0.2 mm thick Teflon coating along its entire length to prevent contamination of the GdLS. The anchors made by Teflon and acrylic are glued on the inner surface of the acrylic vessel in the CD. The cable passes through the anchors and can be pulled in either direction by two stepper motors to deploy the radioactive source along the track of the cable in the detector as shown in Fig. 3. The positions of the anchors are optimized so that we can use limited calibration positions along the cable to obtain comprehensive information about the non-uniformity response of the detector. When the calibration is completed, the radioactive

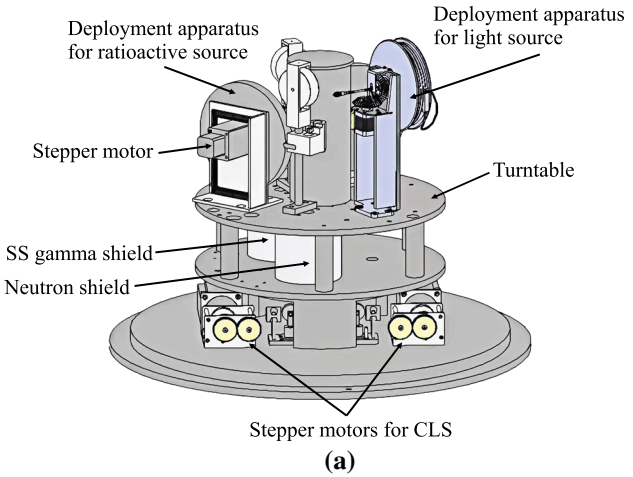

Fig. 2 **a** Automated calibration system. **b** Design of ^{68}Ge source (left) and combined radioactive source (right). The combined source contains multiple gamma sources (^{137}Cs, ^{54}Mn, ^{40}K, ^{60}Co) and one neutron source (^{241}Am-^{13}C)

source is pulled inside the ACU. The limit switch is used to align the radioactive source to the zero position. The load cell is used to monitor the tension of the stainless steel cable to avoid breaking or loosening.

2.3 Simulation software

The simulation software of TAO is based on the framework SNiPER [15] and the Geant4 (10.04.p02) [16] simulation software. It contains the geometry of the TAO detector, the optical parameters, and the list of physics processes. The optical parameters of GdLS, such as the absorption and re-emission probability, are taken from Daya Bay [17] since they use similar GdLS and these optical parameters have been measured to be unchanged at $-50\,^{\circ}$C compared to that

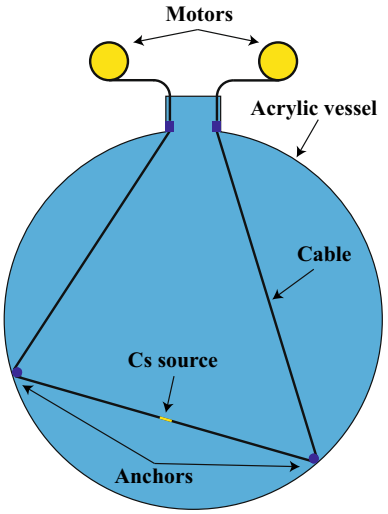

Fig. 3 Schematic of the CLS. The CLS contains two motors, two anchors glued on the inner surface of the acrylic vessel, and one cable. The radioactive source (^{137}Cs) is plated on a small area of the stainless steel cable. The cable passes through the anchors and can be pulled in either direction by two stepper motors to deploy the radioactive source along the track of the cable in the detector

at room temperature [18]. The light yield of the TAO GdLS is measured to be 96% of the JUNO LS at room temperature and increases by 9% at $-50\,^{\circ}$C [19]. The "Livermore Low Energy" model is used to describe the electromagnetic physical processes for photons, electrons, hadrons, and ions [20]. Electronics effects are not included in the simulation since the hardware has not yet been fully tested.

3 Calibration sources

The radioactive sources and reaction processes considered in the calibration are listed in Table 1. In this section, we discuss details about the calibration sources, such as the selection of the radioactive source activities, the selection criteria of calibration events, and the fitting algorithm for the visible energy spectra of the radioactive sources. The visible energy of an event is defined as

$$E_{\mathrm{vis}} = N_{\mathrm{PE}}/Y_0, \tag{1}$$

where N_{PE} is the number of photo-electrons detected by the SiPMs, and Y_0 is the photo-electron yield, which is determined to be 4445 PE/MeV by simulating the neutron capture on hydrogen at the CD center and dividing the average detected PEs by the gamma energy 2.22 MeV.

3.1 Calibration sources carried by ACU

As mentioned in Sect. 2.2, ^{137}Cs, ^{54}Mn, ^{40}K, ^{60}Co, and ^{241}Am-^{13}C are put into one source enclosure, called the

Table 1 List of radioactive sources and processes used for the TAO calibration

Source or process	Type	Radiation	Activity [Bq]	Half life
^{137}Cs (ACU)	γ	0.662 MeV	50	30.1 years
^{54}Mn	γ	0.835 MeV	50	0.85 year
^{60}Co	γ	$1.173MeV + 1.333MeV$	10	5.27 years
^{40}K	γ	1.461 MeV	10	1.25×10^9 years
^{68}Ge	e^+	Annihilation $0.511MeV + 0.511MeV$	500	0.74 year
^{241}Am-^{13}C	n, γ	Neutron + 6.13 MeV (^{16}O*)	2 (neutron)	432 years
$n(p, \gamma)d$	γ	2.22 MeV	2 (neutron)	
^{137}Cs (CLS)	γ	0.662 MeV	500	30.1 years
^{12}B	e	13.4 MeV (end point energy)		20.2 ms

"combined source", and ^{68}Ge is put into another source enclosure.

The ^{68}Ge can emit positron which then annihilates in the source enclosure to release two 0.511 MeV gammas. The ^{68}Ge is separated from other radioactive isotopes because it has a half-life of only 271 days and needs to be replaced after three years. The simulated visible energy spectrum of ^{68}Ge is shown in Fig. 4a. An energy loss tail arises in the visible energy spectrum because gamma particles may deposit some of their energy in non-scintillating materials such as the source enclosure, weights, etc. For this kind of single calibration source, we use a Gaussian function to model the fully absorbed peak and a complementary error function with a normalization parameter to model the energy loss tail. The fitting function is

$$f(E_{\text{vis}}; \eta_0, \eta_1, \mu, \sigma) = \eta_0 \cdot \left(e^{-\frac{(E_{\text{vis}}-\mu)^2}{2\sigma^2}} + \eta_1 \cdot \text{erfc}\left(\frac{E_{\text{vis}} - \mu}{\sqrt{2}\sigma} \right) \right), \quad (2)$$

where erfc is the complementary error function, and μ and σ represent the mean and standard deviation of the visible energy spectrum of the fully absorbed peak. η_0 is the absolute amplitude of the fully absorbed peak while η_1 is the relative amplitude of the energy loss tail.

The ^{241}Am-^{13}C source can release neutrons with kinetic energy less than 100 keV through the ^{13}C(α,n)^{16}O reaction. The ^{16}O may be in a second excited state and de-excites with the release of 6.13 MeV gamma [8]. When the combined source parks in the ACU, neutrons from ^{241}Am-^{13}C may pass through the shield and enter the central detector. To reduce these neutron backgrounds to an acceptable level, the neutron rate of ^{241}Am-^{13}C is chosen to be 2 Bq [21]. Signals from ^{241}Am-^{13}C are selected as prompt-delayed pairs with the accidental backgrounds being removed by the offset-window method [22]. The ^{16}O* de-excitation gamma produces the prompt signal and the neutron capture peak gives the delayed signal. This prompt-delayed coincidence distinguishes the signals of the ^{241}Am-^{13}C source from other signals generated by gammas in the combined source. In GdLS, neutron capture mainly happens on the Gd nucleus (n-Gd) and the H nucleus (n-H). Neutron capture on the Gd nucleus will emit multiple gammas whose energy spectra are complex [23], so only the n-H gamma is used for the non-linearity calibration. Since the energy loss tail of n-Gd events affects the peak of the n-H visible energy spectrum, a function as $\eta_2 + f(E_{\text{vis}}; \eta_0, \eta_1, \mu, \sigma)$ is used to model the visible energy spectrum around the n-H fully absorbed peak, where η_2 models the energy loss tail of the n-Gd spectrum.

The activities of ^{137}Cs, ^{54}Mn, ^{40}K, ^{60}Co are optimized so that the energy loss tail of one source won't form a significant background for the fully absorbed peaks of other sources, as shown in Fig. 4b. Given the activities we choose, the tails of the ^{40}K and ^{60}Co spectra have little impact on the spectra of ^{137}Cs and ^{54}Mn. Therefore, the spectra of ^{54}Mn and ^{137}Cs are fitted together with one function to account for the overlapping in the spectra, and the spectra of ^{40}K and ^{60}Co are fitted together with another function as shown in Fig. 4b. The natural abundance of ^{40}K is about 0.012% [24] so that enriched ^{40}K is used to reduce the volume and mass of the radioactive source.

3.2 Calibration source carried by CLS

CLS carries a ^{137}Cs source of about 500 Bq. We can not use ^{68}Ge at CLS because the released positron will pass through the Teflon thin coating, and the visible energy of gammas produced by positron annihilation is mixed with the visible energy of positron kinetic energy. The main branch of ^{137}Cs decay is through beta decay to the excited state of barium, which then de-excites and emits a gamma of 0.662 MeV. The mean half-life of the excited ^{137}Ba is about 2.55 min, and the end-point kinetic energy of the β ray is about 0.518 MeV, so the 0.662 MeV gamma ray can be distinguished from the β ray.

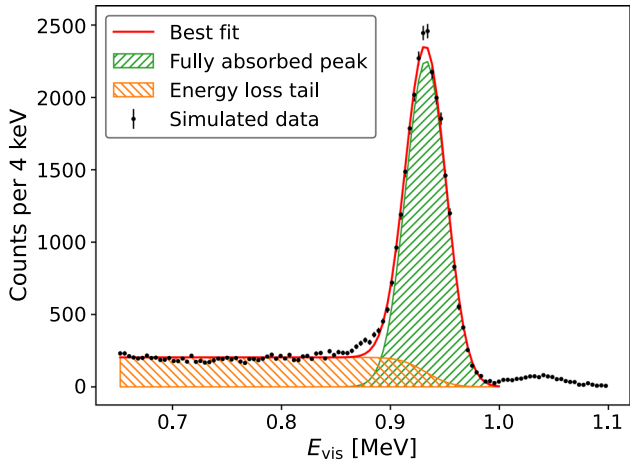

(a)

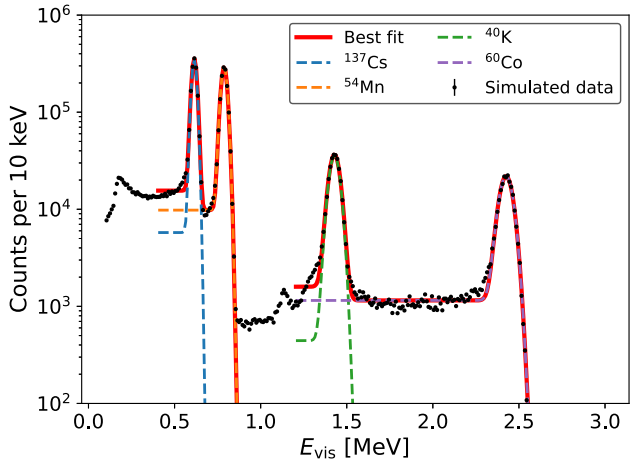

(b)

Fig. 4 **a** The simulated visible energy spectrum of ^{68}Ge. The number of ^{68}Ge events is equivalent to 100 s calibration data. The contributions of the fully absorbed peak and the energy loss tail are shown in the figure. The mean value of the fully absorbed peak is not equal to 1.022 MeV due to the physics non-linearity. **b** Gamma spectra and the fitting results of the radioactive isotopes in the combined source. The number of combined source events is equivalent to 10 h calibration data. The spectra of ^{137}Cs and ^{54}Mn are fitted separately from the spectra of ^{40}K and ^{60}Co

3.3 Cosmogenic ^{12}B

Cosmogenic ^{12}B events can be used in non-linearity calibration. The simulation shows that the muon rate in the TAO CD is about 330 Hz with the input of the measured muon rate in the experimental hall which is about 1/3 of the ground level. The energetic cosmic muons and their daughters can interact with ^{12}C in GdLS to produce unstable isotopes like ^{12}B [7]. The half-life of ^{12}B is 20.2 ms. About 98.2% of them decays to the ground state of ^{12}C by β-emission with a Q value of 13.4 MeV [25]. Therefore, the ^{12}B events can provide a constraint on the electron non-linearity model, especially in the high energy range. A showering muon which produces neutrons in the detector has much larger probability to produce a ^{12}B together than those muons without a neutron followed. To obtain a clean ^{12}B sample, we first select muons with a neutron followed (neutron-tagged muons). The neutron-tagged muon rate is reduced to less than 1 Hz. Then we select ^{12}B candidates within a (5 ms, 50 ms) time window after the muon [8]. The accidental backgrounds can be evaluated by the offset-window method and then be subtracted. About 10^5 ^{12}B events can be selected in the FV in three years. About 2.8% ^{12}N decay events are mixed into the energy spectrum of ^{12}B. The impact on the physics non-linearity is less than 0.05% when ^{12}N events are taken into consideration. For simplicity, ^{12}N events are ignored in this study.

4 Non-uniformity calibration

When particles interact with the GdLS in the CD at different positions, the detector responses are different. This is referred to as the non-uniformity of the detector. The detector non-uniformity $g(r, \theta, \phi)$ is defined as the photo-electron yield at a given position relative to the photo-electron yield at the center of the detector, where r, θ, and ϕ are the radius, polar angle and azimuthal angle of the given position in spherical coordinates, respectively. The origin of the spherical coordinate is at the center of the CD, and the zenith points upwards, as shown in Fig. 1. The non-uniformity of the detector degrades the energy resolution and should be understood well.

To understand how well the non-uniformity $g(r, \theta, \phi)$ can be calibrated, we first simulate the detector responses with 1 MeV electrons at given positions in the detector to extract the true non-uniformity map as the reference. Then we simulate the detector responses with gamma sources deployed at a limited number of positions and calibrate the non-uniformity. The location of the CLS anchors and selection of the calibration points are optimized by comparing the non-uniformity calibration and the reference. Once the non-uniformity $g(r, \theta, \phi)$ is obtained, the visible energy can be evaluated with

$$E_{\text{vis}}^{\text{prompt}}(r, \theta, \phi) = \frac{N_{\text{PE}}}{g(r, \theta, \phi) \cdot Y_0}. \quad (3)$$

4.1 Ideal non-uniformity map

To obtain the reference non-uniformity $g(r, \theta, \phi)$, electrons with a kinetic energy of 1 MeV are simulated at 1364 vertices. These vertices are located on a grid with 20 mm spacing in the r-direction and 6° in the θ-direction. The electron is nearly a point source because it deposits energy in a volume within a radius of a few millimeters, which is much smaller than gamma. Since the detector is approximately symmetric rotationally, we assume $g(r, \theta, \phi) \approx g(r, \theta)$. The full non-

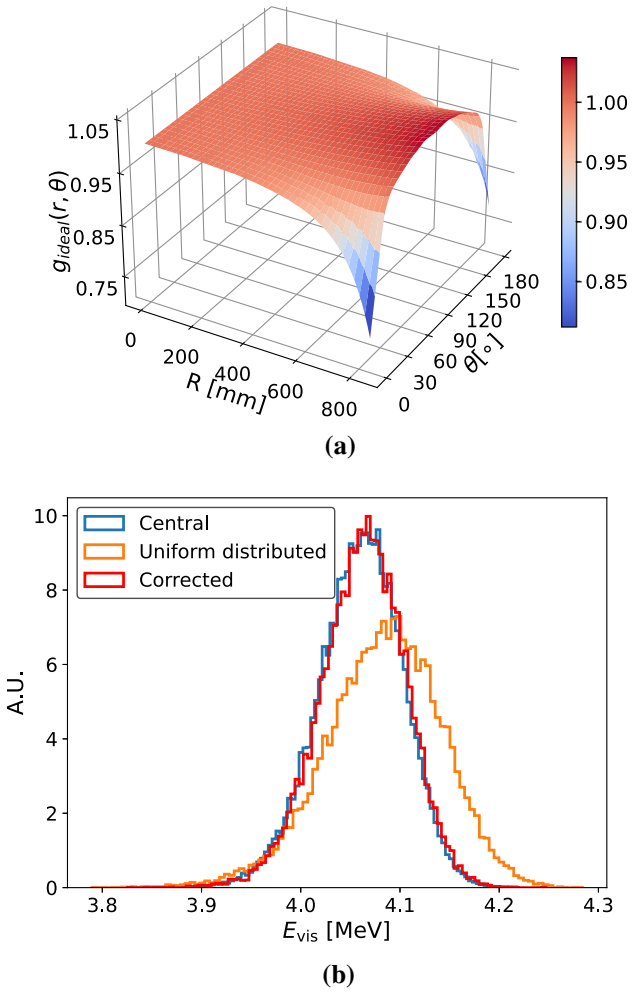

Fig. 5 **a** 3D surface of $g_{\text{ideal}}(r,\theta)$ obtained by simulations of the electrons with a kinetic energy of 1 MeV at many vertices in the detector. **b** E_{vis} spectrum of the positrons with a kinetic energy of 3 MeV. The blue line is the E_{vis} spectrum of the positrons at the detector center. The orange line is the E_{vis} spectrum of the uniformly distributed positrons. the red line is the E_{vis} spectrum corrected with the non-uniformity $g_{\text{ideal}}(r,\theta)$ for the uniformly distributed positrons

uniformity map shown in Fig. 5a is obtained with the Clough–Tocher two-dimension interpolation [26–28]. We refer to this reference non-uniformity map as $g_{\text{ideal}}(r,\theta)$.

Simulation shows that the $g_{\text{ideal}}(r,\theta)$ can correct the non-uniformity of IBD positron well. We simulate the IBD events uniformly distributed within the CD and a set of the events at the CD center, then reconstruct the uniformly distributed events with Eq. (3). Figure 5b is an example for positrons with a kinetic energy of 3 MeV. The difference between the reconstructed positron energy spectrum and the positron energy spectrum at the detector center is small. The relative difference between their central values and the relative energy resolution difference ($\Delta\sigma/E$) are less than 0.15% and 0.01%, respectively. This conclusion is applicable to the positrons in the kinetic energy range from 0 to 8 MeV.

4.2 Optimizing the finite-point uniformity calibration

In this section, we optimize the layout of the CLS system and select a set of deployment calibration points to obtain a good approximation of $g_{\text{ideal}}(r,\theta)$. The optimization results also feed back to the calibration system design.

4.2.1 Optimize the anchor locations

As shown in Fig. 5a, $g_{\text{ideal}}(r,\theta)$ is almost symmetric with respect to the plane of $\theta = 90°$. To be more specific, $|g_{\text{ideal}}(r,\theta) - g_{\text{ideal}}(r,180°-\theta)|/g_{\text{ideal}}(r,\theta)$ is less than 0.2% within the FV thanks to the symmetric arrangement of the SiPMs and the symmetry of the acrylic vessel. A minor asymmetry comes from the different sizes of two holes at two poles of the acrylic vessel. It is safe to assume $g(r,\theta) = g(r,180°-\theta)$ within a precision of 0.2%.

When the locations of the two anchors are fixed, we select very dense points $\vec{P}_{\text{calib}}$ that can be reached by the calibration system and calculate $g_{\text{ideal}}(\vec{P}_{\text{calib}})$. Then, the Clough–Tocher two-dimension interpolator is applied to obtain $g_{\text{calib}}(r,\theta;\theta_1,\theta_2,\phi_2)$, where θ_1, θ_2 and ϕ_2 represent the locations of two anchors. Since we assume that the detector is rotationally symmetric with respect to the z-axis, we set $\phi_1 = 0$ where ϕ_1 is the azimuthal angle of one anchor. In order to optimize the locations of the anchors, a penalty function

$$L(\theta_1,\theta_2,\phi_2) = \int_{S_R} (g_{\text{ideal}}(r,\theta) - g_{\text{calib}}(r,\theta;\theta_1,\theta_2,\phi_2))^2 \cdot dV \tag{4}$$

is defined to evaluate the difference between $g_{\text{ideal}}(r,\theta)$ and $g_{\text{calib}}(r,\theta;\theta_1,\theta_2,\phi_2)$, where S_R means a spherical volume whose radius is smaller than R. R is set to be 700mm to include the FV with a radius less than 650 mm. Besides, limitations of $\theta_1 > 90°$ and $\theta_2 > \theta_1$ are added to allow the installation and positioning of the anchors to be more convenient. We obtain $\theta_1 \approx 102.5°$, $\theta_2 \approx 155.2°$, $\phi_2 \approx 151.7°$ by minimizing $L(\theta_1,\theta_2,\phi_2)$.

4.2.2 Determine suitable calibration points

Once the locations of the two anchors are determined, the track of the CLS cable is fixed. Only limited calibration points along the track of the CLS cable can be used, considering the limitation of the calibration time. The criterion to select suitable calibration points is to set more calibration points where the modulus of the gradient of $g(r,\theta)$ is larger. For the ACU system, we set a calibration point every 100mm in the area with a radius less than or equal to 500mm, and set a calibration point every 50 mm in the area with a radius of 500 mm to 850 mm. For the CLS system, to begin with the starting point of the CLS cable ($\vec{P}_0$), we add a calibration point ($\vec{P}_i$)

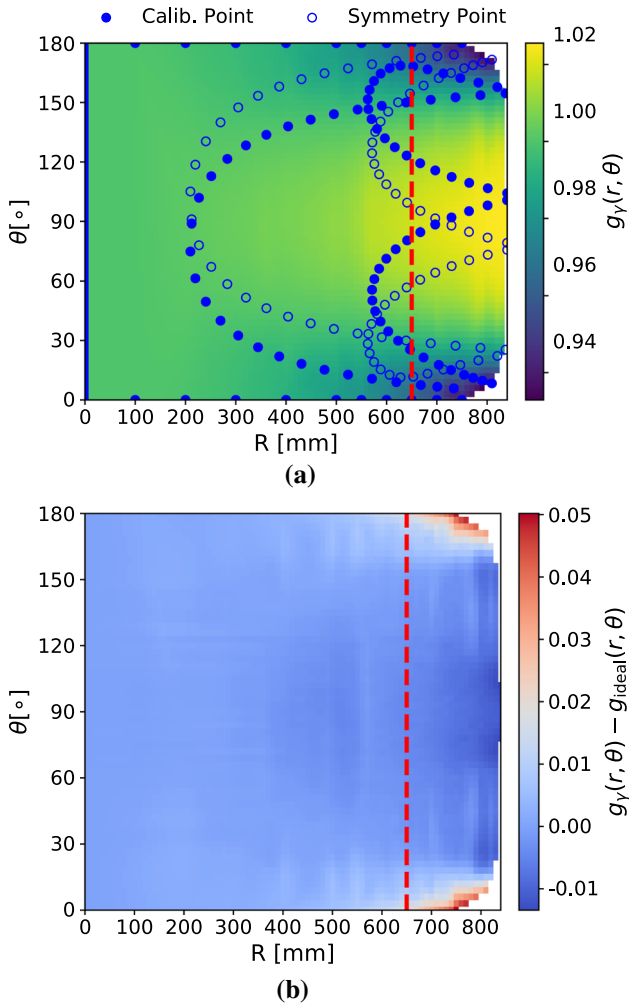

Fig. 6 **a** $g_\gamma(r,\theta)$ interpolated from the ^{68}Ge and ^{137}Cs calibration data. Solid circles are real calibration points. Hollow circles are the symmetry points of the solid circles with respect to z = 0 plane. The point at the detector center is shown as a line from $\theta = 0°$ to $\theta = 180°$ at R = 0 mm. **b** $g_\gamma(r,\theta) - g_{\text{ideal}}(r,\theta)$. The red line is the boundary of the FV

when conditions $0.01 \leq |g_{\text{ideal}}(\vec{P}_i) - g_{\text{ideal}}(\vec{P}_{i-1})|$ and 25 mm $\leq |\vec{P}_i - \vec{P}_{i-1}|$ are met at the same time, or when condition 50 mm $\leq |\vec{P}_i - \vec{P}_{i-1}|$ is met. The starting point $\vec{P}_0$ is marked in Fig. 1. In total, 110 points for non-uniformity calibration are selected and shown as the solid points in Fig. 6a.

4.3 Verification of the calibration

We plan to use the ^{68}Ge and the ^{137}Cs on the ACU and the ^{137}Cs on the CLS to perform the non-uniformity calibration. We can obtain the photo-electron yield relative to the center for a given calibration point and radioactive source on the ACU or CLS. For example, for a given calibration point on the CLS, we place the ^{137}Cs there and obtain the photo-electron yield, then divide it by the photo-electron yield of ^{137}Cs at the detector center. Then we use the Clough–Tocher two-dimension interpolation to obtain the $g(r,\theta)$, as shown in Fig. 6a. Since this non-uniformity map is obtained using gamma sources, it is marked as $g_\gamma(r,\theta)$. Near two poles of the acrylic vessel, the total absorption energy peaks can not be fitted due to the large energy loss effect. This results in missing values near the regions corresponding to the two poles of the acrylic vessel in Fig. 6a. The difference between $g_\gamma(r,\theta)$ and $g_{\text{ideal}}(r,\theta)$ is less than 0.01 in most areas, and the difference is larger near the two poles of the acrylic vessel, as shown in Fig. 6b. This difference prevents us from perfectly correcting the effects of non-uniformity, resulting in a residual non-uniformity. The residual non-uniformity, denoted as RN, is defined as

$$\text{RN} = \sqrt{\frac{1}{V_{\text{FV}}} \cdot \int_{\text{FV}} (g_\gamma(r,\theta) - g_{\text{ideal}}(r,\theta) - \overline{\Delta g})^2 \cdot dV}, \tag{5}$$

where V_{FV} is the total volume of FV and

$$\overline{\Delta g} = \frac{1}{V_{\text{FV}}} \cdot \int_{\text{FV}} (g_\gamma(r,\theta) - g_{\text{ideal}}(r,\theta)) \cdot dV. \tag{6}$$

$\overline{\Delta g}$ is about -0.14% and will cause bias of reconstructed visible energy. RN leads to degradation in the resolution of reconstructed visible energy, but it is only about 0.2%, satisfying the requirement of less than 0.5%. Thus, the energy non-uniformity can be well calibrated with the radioactive sources on ACU and CLS.

4.4 Energy resolution

In order to get the energy resolution of the TAO, IBD events are simulated at the center of the CD. For mono-energetic IBD events, we can calculate the standard deviation (σ) and mean of their visible energies ($E_{\text{vis}}^{\text{prompt}}$). The energy resolution of IBD events is defined as $\sigma/E_{\text{vis}}^{\text{prompt}}$ and is shown in Fig. 7a.

Residual non-uniformity and electronics effects such as cross talk, dark noise, charge resolution can cause the energy resolution degradation ($\Delta\sigma/E_{\text{vis}}^{\text{prompt}}$). The energy resolution degradation due to electronics effects is less than 0.23% at 1 MeV, see Ref. [10] for details. To study the energy resolution degradation due to residual non-uniformity, Eq. (3) and $g_\gamma(r,\theta)$ are used to reconstruct uniformly distributed IBD events. Taking the vertex reconstruction resolution into account, a 5 cm Gaussian vertex smearing is added to the true vertex of each simulated event. The reconstructed visible energy spectrum of the IBD events whose reconstructed vertices are within FV is compared with the visible energy spectrum of the central IBD events. It can be seen from Fig. 7a that the energy resolution degradation is less than 0.05%. Fig-

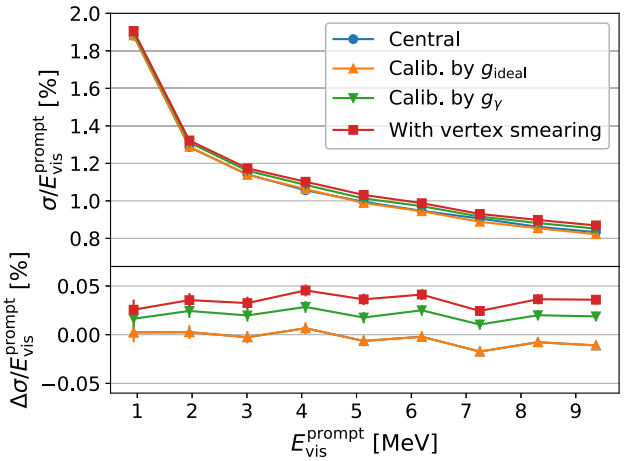

(a)

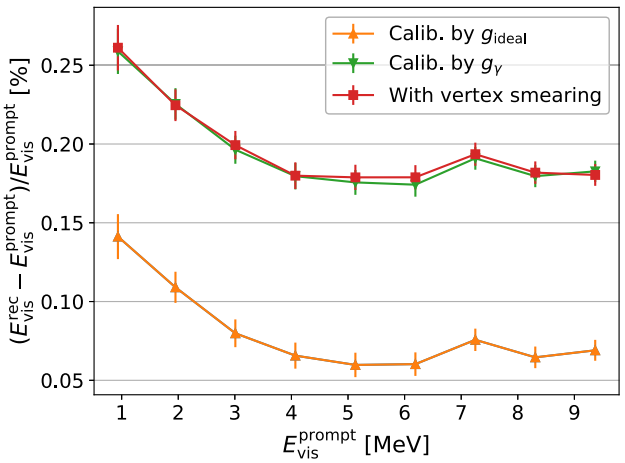

(b)

Fig. 7 **a** Energy resolution of reconstructed IBD prompt events for detector central events, and uniformly distributed events corrected by different non-uniformity maps. For central events, the energy resolution is quite close to the result corrected by g_{ideal} causing some overlaps. **b** E_{vis} bias of reconstructed e^+ spectrum. $E_{\text{vis}}^{\text{prompt}}$ here means visible energy of central IBD prompt events. $E_{\text{vis}}^{\text{rec}}$ is the visible energy of reconstructed IBD prompt events which are distributed uniformly within the FV. Vertex smearing here takes into account a 5 cm vertex resolution

ure 7b shows that the bias of reconstructed energy is smaller than 0.3%.

5 Non-linearity calibration

In this section, we first introduce the non-linearity model. Then the systematic biases and uncertainties of the visible energy of these calibration sources are discussed one by one. Finally, we apply the model to fit the calibration data and obtain the calibration performance.

5.1 Model of physics non-linearity

The visible energy of the prompt event of the IBD reaction can be decomposed as

$$E_{\text{vis}}^{\text{prompt}} = E_{\text{vis}}^{\text{e}} + E_{\text{vis}}^{\text{anni}}, \tag{7}$$

where $E_{\text{vis}}^{\text{e}}$ is the visible energy associated with the positron kinetic energy and $E_{\text{vis}}^{\text{anni}}$ is that of the annihilation gammas. $E_{\text{vis}}^{\text{e}}$ should be equal to the visible energy of an electron with the same kinetic energy, thus can be calibrated with the β decay sources [8]. $E_{\text{vis}}^{\text{anni}}$ can be calibrated with the ^{68}Ge source. The physics non-linearity for an electron or a positron is defined by

$$f_{\text{nonlin}}^{\text{e}} = E_{\text{vis}}^{\text{e}}/E^{\text{e}}, \tag{8}$$

where E^e is the true kinetic energy of the electron or positron.

The physics non-linearity is caused by ionization quenching and the emission of Cherenkov radiation.

Ionization quenching In general, when the particles deposit energy in the GdLS, the solvent molecules are excited, then the energy is transferred to the fluorescent molecules through dipole-dipole interactions [8]. The energy transfer efficiency is reduced, which leads to a non-linearity between the energy converted to scintillation photons (E_{scint}) and the kinetic energy of the electron or positron E^e. This is known as the quenching effect and can be described by the empirical formula known as Birks' law [29]:

$$E_{\text{scint}}(E^{\text{e}}, k_{\text{B}}) = \int_0^{E^{\text{e}}} \frac{dE}{1 + k_{\text{B}} \cdot \frac{dE}{dx}}, \tag{9}$$

where k_{B} is the Birks' constant and dE/dx is the stopping power. dE/dx is obtained from an ESTAR calculation [30] using the TAO liquid scintillator properties.

Cherenkov radiation Cherenkov photons are produced if the phase velocity of light in the medium is less than the velocity of a charged particle [31]. We assume that the number of photo-electrons produced by the Cherenkov radiation is a function of E^e. The function, namely f_{C}, is obtained with the Geant4 simulations as shown in Fig. 8a. f_{C} is set to 1 at 1 MeV while the absolute contribution of the Cherenkov radiation can be determined by the calibration data.

Considering these two contributions, the total non-linearity for the energy deposited by an electron or a positron is defined as:

$$f_{\text{nonlin}}^{\text{e}}(E^{\text{e}}; A, k_{\text{B}}, k_{\text{C}}) = A \cdot \left(\frac{E_{\text{scint}}(E^{\text{e}}, k_{\text{B}})}{E^e} + k_{\text{C}} \cdot \frac{f_{\text{C}}(E^{\text{e}})}{E^{\text{e}}} \right), \tag{10}$$

where A is a normalization factor, and k_{C} is the relative contribution of the Cherenkov light to the scintillation light, both to be determined from the fitting.

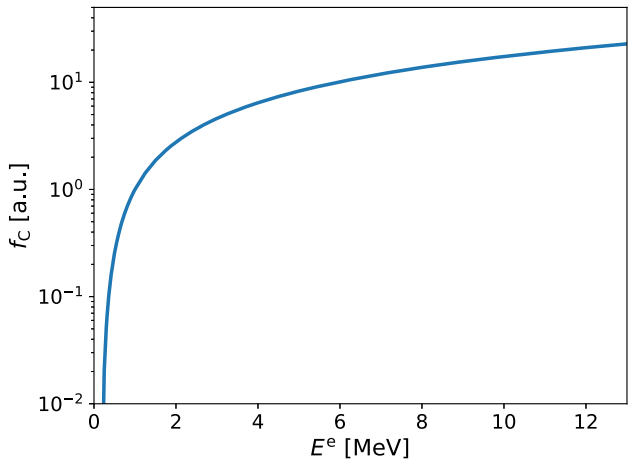

(a)

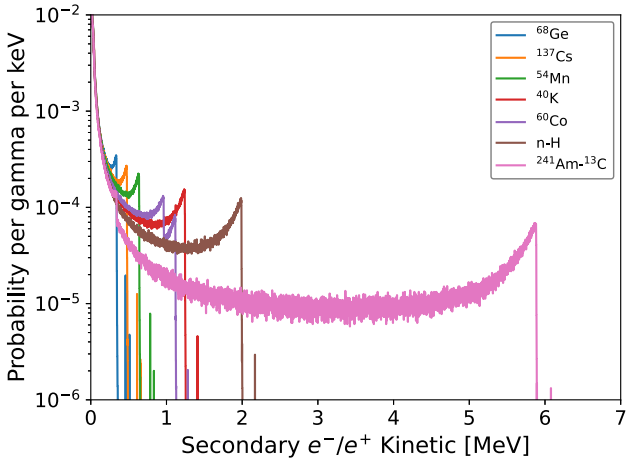

(b)

Fig. 8 **a** Number of photo-electrons produced by the Cherenkov radiation. f_C is set to 1 at 1 MeV and the absolute contribution of the Cherenkov radiation can be determined by the calibration data. **b** The kinetic energy distributions of secondary electrons or positrons for gamma sources

A gamma particle deposits its energy in the LS via secondary electrons. The physics non-linearity of gamma can be written as

$$f^{\gamma}_{\text{nonlin}}(E^e; A, k_B, k_C) \equiv \frac{E^{\gamma}_{\text{vis}}}{E^{\gamma}} = \frac{\int_0^{E_\gamma} P(E^e) \cdot f^e_{\text{nonlin}}(E^e; A, k_B, k_C) \cdot E^e \cdot dE^e}{\int_0^{E_\gamma} P(E^e) \cdot E^e \cdot dE^e}, \tag{11}$$

where $P(E^e)$ denotes the probability density function of a given gamma converting to secondary electrons or/and positrons of kinetic energy E^e via Compton scattering, photoelectric effect, or pair production [9]. $P(E^e)$ is determined with simulations as shown in Fig. 8a.

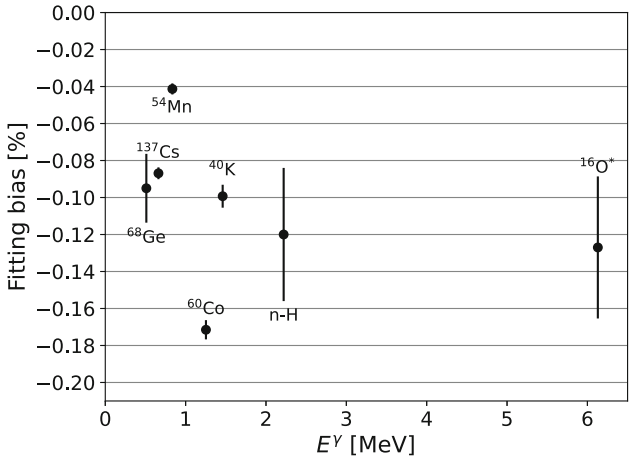

Fig. 9 The fitting bias due to the energy loss effect

As for a continuous spectrum like ^{12}B β-decay, we can also calculate the expected visible energy distribution as

$$P_v(E_{\text{vis}}) = \left(P_k(E^e(E_{\text{vis}})) \cdot \left| \frac{dE^e}{dE_{\text{vis}}} \right| \right) \otimes \text{Res}(E_{\text{vis}}), \tag{12}$$

where $P_v(E_{\text{vis}})$ and $P_k(E^e)$ mean the visible energy and the kinetic energy distributions of the continuous β spectrum respectively, and $\text{Res}(E^e)$ is the energy resolution of the detector. $E^e(E_{\text{vis}})$ can be calculated with Eqs. (8) and (10).

This physics non-linearity model is similar to the model used in the energy calibration of Daya Bay [8] which uses similar GdLS.

5.2 Systematic biases and uncertainties

In this section, we analyze the systematic biases of the visible energy of the calibration sources used in non-linearity calibration. The effects that lead to systematic biases are analyzed one by one. The approach used here is similar to that used in the Daya Bay [8] and JUNO [9] experiments.

5.2.1 Energy loss effect

Gamma particles may deposit some of their energy in non-scintillating materials such as the source enclosure, weights, etc. This results in a tail in the visible energy distribution and might cause a bias in the fit to the fully absorbed peak. For such gamma source, we can apply Eq. (2) to fit its visible energy spectrum as shown in Fig. 4a. The fitted μ value is referred to as $E^{\text{fit}}_{\text{vis}}$. For comparison, events with energy fully absorbed in the GdLS are selected with the Monte Carlo truth information and fitted with a Gaussian. The fitted mean is referred to as $E^{\text{ideal}}_{\text{vis}}$. We define $(E^{\text{fit}}_{\text{vis}} - E^{\text{ideal}}_{\text{vis}})/E^{\text{ideal}}_{\text{vis}}$ as the fitting bias to measure the deviation caused by energy loss.

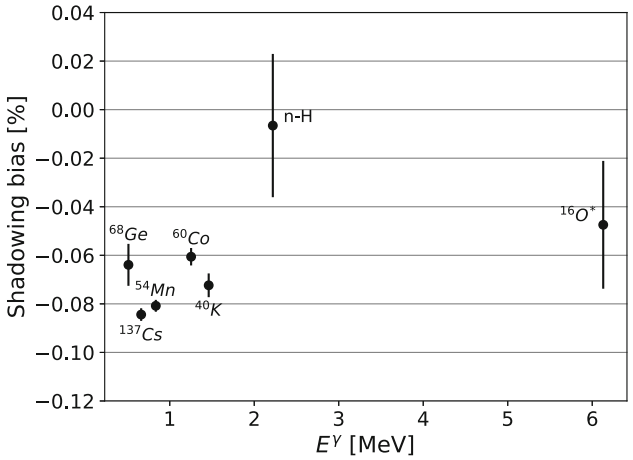

Fig. 10 The shadowing bias due to the absorption of scintillation photons by the surfaces of the source enclosure and weights

As shown in Fig. 9, the fitting bias is less than 0.2% for radioactive sources. The energy loss in the non-scintillating materials is less for higher energy gamma. However, the differences for the gamma sources used here are negligible. We assume that the fitting biases between these gammas are correlated.

5.2.2 Shadowing effect

Scintillation photons could be absorbed or reflected by the source enclosure or the weights. The impact on the calibration is referred to as "shadowing effect". To reduce the absorption, the surfaces of the enclosure and the weights are covered by Polytetrafluoroethylene (PTFE) with high reflectivity [13]. In this study, we assume the reflectivity is 95%.

In order to decouple the shadowing effect from the energy loss effect, only events with energy fully deposited in the GdLS are selected in the simulations. The visible energy spectrum is modeled by a Gaussian function. The fitted mean of the Gaussian is marked as $E_{\mathrm{vis}}^{\mathrm{shadow}}$. For comparison, we also simulate the naked radioactive sources without the enclosure and weights to avoid shadowing effect. The fitted mean is marked as $E_{\mathrm{vis}}^{\mathrm{nos}}$. The bias caused by the shadowing effect is defined as $(E_{\mathrm{vis}}^{\mathrm{shadow}} - E_{\mathrm{vis}}^{\mathrm{nos}})/E_{\mathrm{vis}}^{\mathrm{nos}}$. As shown in Fig. 10, the shadowing bias of each radioactive source is smaller than 0.1%. We assume that the shadowing biases are correlated among different radioactive sources because they are caused by the similar enclosures and weights.

5.2.3 ^{16}O 6.13 MeV gamma bias*

When the ^{241}Am-^{13}C source releases a gamma of 6.13 MeV, it also releases a neutron of a kinetic energy of less than 100 keV [8]. While the neutron capture signal is delayed due to the neutron thermalization process thus separated from the 6.13 MeV gamma, the proton recoil caused by this neutron produces a small amount of scintillation light and overlaps with the gamma. The amount of the scintillation light relies on the neutron scattering process and varies event by event. This introduces about 0.4% bias to the calibration using the 6.13 MeV gamma.

5.2.4 Residual bias after non-uniformity correction

The detector response is not uniform. The vertexes of the β decays of the cosmogenic ^{12}B distribute uniformly in the detector. When they are used for calibration, the detector non-uniformity must be corrected. Gammas coming from the calibration sources may not deposit their energy at the position of the sources since a gamma in the MeV energy region has an attenuation length of $\sim$ 20 cm in the liquid scintillator. And the energy is not deposited at a single point. Therefore, the detector non-uniformity also affects the visible energy spectra of gammas. The non-uniformity effect can be corrected but not perfectly. As described in Sect. 4.4, the residual bias after non-uniformity correction can be controlled within 0.3%. It is conservatively taken as a fully correlated bias among different energies.

5.2.5 Instrumental non-linearity

The non-linearity caused by the SiPMs and the electronics readout can be neglected. The scintillation light is detected with 4024 tiles of SiPMs in the TAO CD. Each tile contains 32 SiPMs of 12×6 mm^2 in dimension and is read out with two electronics channels. Each SiPMs contains 12800 Single Photon Avalanche Diodes (SPADs) of 75×75 μm^2 in dimension. There are 1.65×10^9 SPADs in total. They collect about 4500 photo-electrons per MeV for electrons. Therefore, the response of the SiPMs is linear for events in the MeV energy region since the photo-electron multiplicity on a SPAD is a small quantity. The electronics readout of the SiPMs has the good resolution to distinguish the photo-electron multiplicity for several photo-electrons. In average, each electronics channel reads 0.55 photo-electrons per MeV. Therefore, the electronics readout is expected to be linear.

5.2.6 Summary of systematic bias and uncertainty

The effects discussed above are summarized in Table 2. We handle the uncertainties as the calibration strategy in JUNO [9]. We assume that all the biases can be corrected, but with a 100% uncertainty. This means that the uncertainty is assumed to be 100% of the absolute value of the corresponding bias. The uncertainties are further separated into either "correlated" at different energies, or "single point", depending on how they would move individual energy points up and down. For example, the uncertainties due to the shadowing effects

are correlated among different sources. On the other hand, the bias due to 6.13 MeV gamma is independent from the others (single point). Different types of uncertainties have different impacts on the non-linearity fitting in the next section.

5.3 Non-linearity fitting

As planned, a non-linearity calibration will be performed once a month. At each calibration time, the ^{68}Ge source will be placed in the center of the detector for 100 s, and the combined source will be placed in the center of the detector for 10 h due to the low activity of the neutron source. Therefore, we simulated one set of calibration data to verify the effectiveness of the calibration strategy. Besides, 10^5 ^{12}B events that can be collected in FV in three years are simulated. Equation (3) is used to reconstruct the visible energy of each event. ^{12}B events below 3 MeV are not used due to high background contamination in this range. For simplicity, ^{12}B events from 12 MeV to 14 MeV are also ignored because there are about 30% ^{12}N events in this energy range [8].

To fit the detector energy non-linearity with the model shown in Eq. (11), a χ^2 is defined as:

$$\chi^2 = \sum_{i=1}^{7} \left(\frac{M_i^\gamma - P_i^\gamma}{\sigma_i} \right)^2 + \sum_{j=1}^{90} \frac{\left(M_j^{^{12}\mathrm{B}} - P_j^{^{12}\mathrm{B}} \right)^2}{M_j^{^{12}\mathrm{B}}}, \qquad (13)$$

where M_i^γ and P_i^γ are measured and predicted visible energy peaks of gamma sources, respectively. σ_i contains statistical and systematic uncertainties of M_i^γ. The systematic uncertainties are listed in Table 2. In the energy range from 3 MeV to 12 MeV, the energy spectrum of ^{12}B is equally divided into 90 bins. $M_j^{^{12}\mathrm{B}}$ and $P_j^{^{12}\mathrm{B}}$ are the numbers of ^{12}B events measured and predicted with Eq. (12) in the j-th bin, respectively. In the regular calibration of each month, only the first term in Eq. (13) is used in the fitting, and when 10^5 ^{12}B events are accumulated, the second item is included. Minimizing the χ^2, we obtain the best fit values of the non-linearity model parameters A, k_B and k_C in Eq. (11). The fitting results are shown in Fig. 11. The difference between the fitted E_vis^γ and the simulated E_vis^γ is less than 0.2%.

To calculate the 68% confidence interval of the best fit non-linearity, we sample the visible energy of γs and ^{12}B β decays according to the statistical uncertainty and the systematic uncertainties listed in Table 2. For a correlated uncertainty, a random number that obeys the normal distribution is generated and is multiplied by the uncertainty to calculate the offsets for the visible energies of all relevant calibration sources. For the single point uncertainty, the data point is shifted independently. We repeat this procedure 5000 times and fit each set of data to get the electron non-linearity curves. Finally, we get the 68% confidence interval for the physics non-linearity as shown in Fig. 12.

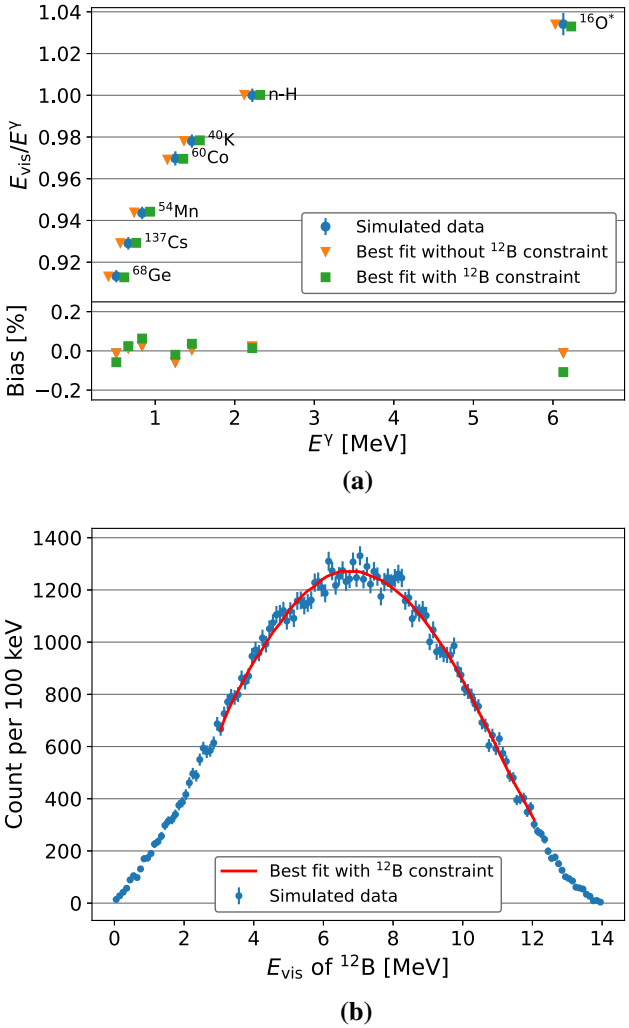

Fig. 11 **a** The best fit points of the radioactive gamma sources compared with the simulated data points. There are two fitting cases on the plot, namely with and without the ^{12}B constraint. The fitted data points are shifted horizontally for visibility. **b** Best fit and simulated ^{12}B spectra. The total number of ^{12}B events is about 10^5, which can be collected in FV in 3 years of data taking

For comparison, mono-energetic electrons are simulated at the CD center to obtain the true inherent non-linearity, as shown in Fig. 12. For the situation without the ^{12}B data constraint, the best fit curve and the inherent non-linearity agree within 0.2% in the energy range from 0.5 MeV to 8 MeV. The uncertainty of the best fit curve is less than 0.6% in the same energy range, better than our requirement of less than 1% uncertainty. For the situation with the constraint of three years of ^{12}B data, the uncertainty is less than 0.4%.

6 Conclusion

A calibration strategy for the TAO detector has been developed to understand its non-uniformity and physics non-

Table 2 A list of systematic biases and uncertainties. The uncertainties are assumed to be 100% of the absolute values of the biases. The last column indicates whether the biases and uncertainties are correlated between different sources or energies

Source	Bias	Uncertainty	Type
Energy loss effect	-0.2% to -0.04%	$< 0.2\%$	Correlated
Shadowing effect	-0.1% to 0%	0.1%	Correlated
^{16}O* 6.13 MeV γ uncertainty	$+0.4\%$	0.4%	Single point
Instrumental non-linearity	~ 0	~ 0	
Position-dependent effect	$< 0.3\%$	0.3%	Correlated

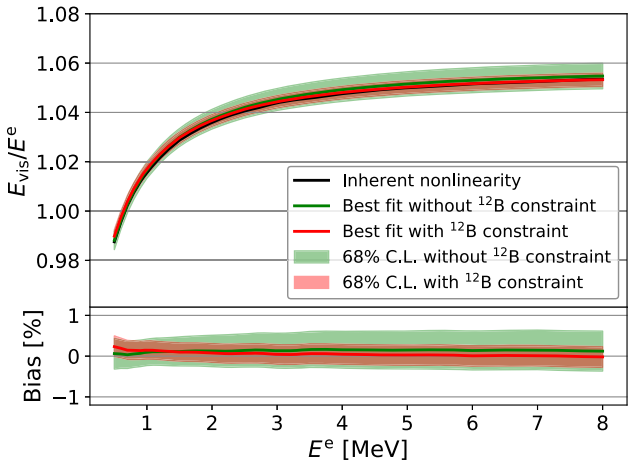

Fig. 12 Electron non-linearity fitting results. E^e is the kinetic energy of the electron or positron. The black line is the true inherent non-linearity. The green line and band are the best fit and the 68% confidence interval without the constraint from the ^{12}B spectrum. The red line and band are the best fit and the 68% confidence interval with the constraint from the ^{12}B spectrum

linearity. The TAO detector contains two independent calibration systems called the ACU and CLS. The ACU is capable to carry two radioactive sources and one LED source and deploys one of them into the detector along the central vertical axis at each time, while the CLS is designed to carry a single radioactive source that can be deployed to off-axis positions. For non-uniformity, we utilize the ACU and CLS to deploy radioactive sources to 110 positions to study the detector response, then generate a map to correct the detector non-uniformity. After the correction, the residual non-uniformity is less than 0.2%. The energy resolution degradation and energy bias caused by the residual non-uniformity can be controlled within 0.05% and 0.3% respectively. For the physics non-linearity, we utilize several gamma sources with energies ranging from a few hundred keV to several MeV to control the uncertainty within 0.6% for electron or positron with kinetic energy greater than 0.5 MeV. ^{12}B events can be used to reduce the uncertainty of physics non-linearity down to 0.4% assuming statistics collected in three years of data taking. With this calibration strategy, TAO is projected to measure high-precision reactor antineutrino energy spectrum.

Acknowledgements This work is supported by the National Natural Science Foundation of China under Grant Number 12022505, 11875282 and 11775247, the joint RSF-NSFC project under Grant Number 12061131008, the Youth Innovation Promotion Association of Chinese Academy of Sciences, and by the Program of the Ministry of Education and Science of the Russian Federation for higher education establishments with project Number FZWG-2020-0032 (2019-1569). We gratefully acknowledge help from Jianglai Liu, Yue Meng, Feiyang Zhang, Zeyuan Yu, and Miao Yu.

Data Availability Statement This manuscript has no associated data or the data will not be deposited. [Authors' comment: The data can be provided upon request to the corresponding author.]

Funded by SCOAP^3. SCOAP^3 supports the goals of the International Year of Basic Sciences for Sustainable Development.

References

1. C.L. Cowan, F. Reines, F.B. Harrison, H.W. Kruse, A.D. McGuire, Detection of the free neutrino: a confirmation. Science **124**, 103–104 (1956). https://doi.org/10.1126/science.124.3212.103
2. M. Apollonio et al., Search for neutrino oscillations on a long baseline at the CHOOZ nuclear power station. Eur. Phys. J. C **27**, 331–374 (2003). https://doi.org/10.1140/epjc/s2002-01127-9. arXiv:hep-ex/0301017
3. S. Abe et al., Precision measurement of neutrino oscillation parameters with KamLAND. Phys. Rev. Lett. **100**, 221803 (2008). https://doi.org/10.1103/PhysRevLett.100.221803. arXiv:0801.4589,
4. F.P. An et al., Observation of electron-antineutrino disappearance at Daya Bay. Phys. Rev. Lett. **108**, 171803 (2012). https://doi.org/10.1103/PhysRevLett.108.171803. arXiv:1203.1669,

5. J.K. Ahn et al., Observation of reactor electron antineutrino disappearance in the RENO experiment. Phys. Rev. Lett. **108**, 191802 (2012). https://doi.org/10.1103/PhysRevLett.108.191802. arXiv:1204.0626
6. Y. Abe et al., Indication of reactor $\bar{\nu}_e$ disappearance in the double Chooz experiment. Phys. Rev. Lett. **108**, 131801 (2012). https://doi.org/10.1103/PhysRevLett.108.131801. arXiv:1112.6353,
7. F.P. An et al., Neutrino physics with JUNO. J. Phys. G **43**(3), 030401 (2016). https://doi.org/10.1088/0954-3899/43/3/030401. arXiv:1507.05613
8. D. Adey et al., A high precision calibration of the nonlinear energy response at Daya Bay. Nucl. Instrum. Meth. A **940**, 230–242 (2019). https://doi.org/10.1016/j.nima.2019.06.031. arXiv:1902.08241
9. A. Abusleme et al., Calibration strategy of the JUNO experiment. JHEP **03**, 004 (2021). https://doi.org/10.1007/JHEP03(2021)004. arXiv:2011.06405,
10. A. Abusleme et al., TAO conceptual design report: a precision measurement of the reactor antineutrino spectrum with sub-percent energy resolution. arXiv:2005.08745
11. J. Liu et al., Automated calibration system for a high-precision measurement of neutrino mixing angle θ_{13} with the Daya Bay antineutrino detectors. Nucl. Instrum. Meth. A **750**, 19–37 (2014). https://doi.org/10.1016/j.nima.2014.02.049. arXiv:1305.2248
12. J. Hui et al., The automatic calibration unit in JUNO. JINST **16**(08), T08008 (2021) https://doi.org/10.1088/1748-0221/16/08/T08008. arXiv:2104.02579
13. F. Neves, A. Lindote, A. Morozov, V. Solovov, C. Silva, P. Bras, J.P. Rodrigues, M.I. Lopes, Measurement of the absolute reflectance of polytetrafluoroethylene (PTFE) immersed in liquid xenon. JINST **12**(01), P01017 (2017). https://doi.org/10.1088/1748-0221/12/01/P01017. arXiv:1612.07965
14. Y. Zhang, J. Hui, J. Liu, M. Xiao, T. Zhang, F. Zhang, Y. Meng, D. Xu, Z. Ye, Cable loop calibration system for Jiangmen underground neutrino observatory. Nucl. Instrum. Meth. A **988**, 164867 (2021). https://doi.org/10.1016/j.nima.2020.164867. arXiv:2011.02183,
15. T. Lin, J. Zou, W. Li, Z. Deng, X. Fang, G. Cao, X. Huang, Z. You, The application of SNiPER to the JUNO simulation. J. Phys. Conf. Ser. **898**(4), 042029 (2017). https://doi.org/10.1088/1742-6596/898/4/042029. arXiv:1702.05275
16. S. Agostinelli et al., GEANT4-A simulation toolkit. Nucl. Instrum. Meth. A **506**, 250–303 (2003). https://doi.org/10.1016/S0168-9002(03)01368-8
17. F.P. An et al., A side-by-side comparison of Daya Bay antineutrino detectors. Nucl. Instrum. Meth. A **685**, 78–97 (2012). https://doi.org/10.1016/j.nima.2012.05.030. arXiv:1202.6181
18. Z. Xie, J. Cao, Y. Ding, M. Liu, X. Sun, W. Wang, Y. Xie, A liquid scintillator for a neutrino detector working at −50 degree. Nucl. Instrum. Meth. A **1009**, 165459 (2021). https://doi.org/10.1016/j.nima.2021.165459. arXiv:2012.11883,
19. Z. Xie, Research and development of key detection technologies of the tao experiment, Ph.D. thesis. Institute of High Energy Physics, Chinese Academy of Sciences (2022)
20. S. Agostinelli et al., Physics Reference Manual, Version: geant4 9 (0)
21. J. Liu, R. Carr, D.A. Dwyer, W.Q. Gu, G.S. Li, R.D. McKeown, X. Qian, R.H.M. Tsang, F.F. Wu, C. Zhang, Neutron calibration sources in the Daya Bay experiment. Nucl. Instrum. Meth. A **797**, 260–264 (2015). https://doi.org/10.1016/j.nima.2015.07.003. arXiv:1504.07911
22. F.P. An et al., Measurement of electron antineutrino oscillation based on 1230 days of operation of the Daya Bay experiment. Phys. Rev. D **95**(7), 072006 (2017). https://doi.org/10.1103/PhysRevD.95.072006. arXiv:1610.04802
23. D. Adey et al., Improved measurement of the reactor antineutrino flux at Daya Bay. Phys. Rev. D **100**(5), 052004 (2019). https://doi.org/10.1103/PhysRevD.100.052004. arXiv:1808.10836
24. H. Leutz, G. Schulz, H. Wenninger, The decay of potassium-40. Z. Phys. **187**(2), 151–164 (1965). https://doi.org/10.1007/BF01387190
25. J. Kelley, J. Purcell, C. Sheu, Energy levels of light nuclei a=12. Nucl. Phys. A **968**, 71–253 (2017). https://doi.org/10.1016/j.nuclphysa.2017.07.015
26. P. Alfeld, A trivariate Clough–Tocher scheme for tetrahedral data. Comput. Aid. Geom. Design **1**(2), 169–181 (1984). https://doi.org/10.1016/0167-8396(84)90029-3
27. G.M. Nielson, A method for interpolating scattered data based upon a minimum norm network. Math. Comput. **40**(161), 253–271 (1983). https://doi.org/10.2307/2007373
28. R. Renka, A. Cline, A triangle-based C^1 interpolation method. Rocky Mt. J. Math. **14**(1), 223–238 (1984). https://doi.org/10.1216/RMJ-1984-14-1-223
29. J.B. Birks, The Theory and Practice of Scintillation Counting: International Series of Monographs in Electronics and Instrumentation, vol. 27. Elsevier (2013). https://doi.org/10.1016/C2013-0-01791-4
30. M.J. Berger et al., ESTAR, PSTAR, and ASTAR: computer programs for calculating stopping-power and range tables for electrons, protons, and helium ions (version 1.2.3). http://physics.nist.gov/Star
31. P.A. Cherenkov, Visible luminescence of pure liquids under the influence of γ-radiation. Dokl. Akad. Nauk SSSR **2**(8), 451–454 (1934). https://doi.org/10.3367/UFNr.0093.196710n.0385